

**Revisiting the axisymmetric rotor stator flow in a
cavity of moderate radial aspect ratio : Influence of
curvature and of boundary conditions on outer shroud
and inner hub on the transition and nature of
transition to unsteadiness.**

Gesla, Le Quéré, Duguet, Martin Witowski, order to be defined

LISN

September 28, 2023

1 Introduction and motivation

Owing to their relevance to many engineering configurations or geophysical situations rotating flows are one of the most investigated subjects of the fluid mechanics literature [1], [2]. Their study subdivides in many more specific situations, amongst which turbo-machines related applications have put to the fore flows and related heat transfer between differentially rotating disks of large radial aspect ratio [3]. Early analytical studies have considered disks of infinite radial extension, giving rise to an abundant literature about similarity solutions, their multiplicity and corresponding controversies and disputes. There have been many reviews of these early works (see eg [4], ...) and it is useless to paraphrase here the many developments and debates that have taken place over more than 50 years.

Laboratory experiments aiming at investigating the flow characteristics have considered disks of finite radial extension with variable degrees of confinement which have been shown to have a substantial effect on the selection of classes of similarity solutions. In particular the presence of an outer shroud has been shown to favor Batchelor type flows with two boundary layers on each disk enclosing an inviscid rotating core. Experiments which have considered completely enclosed cavities by an external shroud have had to make a choice of the conditions on the shroud, either attached to the rotor ([5]) or to the stator ([6],[7],[8],[9]). In addition some have used an inner solid hub either rotating as part of the shaft driving the rotating disk ([10],[11]) or attached to the stator [12], all these variations resulting in a great variety of configurations.

One more source of variability for enclosed rotor-stator configurations lies in the so-called corner singularity, which has been dealt with numerically by introducing various types of regularization in particular for numerical algorithms based on the use of Chebyshev spectral approximations ([13], [14]).

Numerous flow visualizations have shown the co-existence of circular axisymmetric rolls and spiral rolls. The Spiral Rolls (SR) are now well understood. They have been shown to originate from a supercritical Hopf bifurcation of the base flow [15], [16]. Their numerical simulation however requires sufficient resolution in the azimuthal direction since their characteristic azimuthal wavenumber is around 30. It was also shown that the range of nonlinearly allowable wavenumbers was limited by an Eckhaus type mechanism.

On the other hand, the origin of the circular rolls has not yet been clearly identified. In

cavities of large aspect ratio ($\frac{R}{H} > 10$) experiments have reported the existence of sustained circular rolls for Reynolds numbers as low as 200 ([7],[8],[9]). Numerical simulations of the axisymmetric equations report on. The first attempt to predict the instability of the base flow (other than through brute force time integration of the unsteady equations) was carried out by Daube and Le Quéré [17]. Using numerical algorithms proposed by Tuckerman [18], they were able to compute the steady solution branch and their spectrum through the use of Arpack. Using a numerical resolution of 600x160 in an aspect ratio 10 cavity, they bracketed the critical Reynolds number in between 2900 and 3000. This value was confirmed through time integration of the linearized equations for different values of the Reynolds number in the neighborhood of Re_c although it was observed that the energy of the fluctuations was amplified by a huge amount ($\simeq 10^{10}$) before achieving their asymptotic behavior, indicating a very large non normality. They also showed the existence of subcritical large amplitude chaotic solutions for Reynolds numbers as low as 2000.

Early numerical simulations aiming at reproducing the large aspect ratio experiments have faced difficulties in approximating the corresponding configurations. In order to get better confidence in the accuracy of the numerical solutions, shorter cavities but still rather large aspect ratio cavities have been considered and performing simulations in cavities of radial aspect ratio 5 has become a standard test case 5 ([19]), [20], [12], [21], [22])

[17], [23]

When investigating issues such as the loss of stability of the enclosed flow or transition to unsteadiness, it is therefore legitimate to ask the question of the influence of these various combinations of boundary conditions on the flow stability. In addition whether the shroud is attached to the rotor or to the stator, there is a discontinuity in the azimuthal velocity component in a corner, which may also have an influence of the stability characteristics.

In order to shed some light on these questions we have computed the stability of the axisymmetric solution in a cavity of radial aspect ratio of 5 extending from an inner radius of 5 to and outer radius of 10. We have considered 4 types of boundary conditions on the inner ou outer radius, fixed (FIX), rotating (ROT), stress free (STF) and linear (LIN), and in total 7 combinations.

2 Configuration and Governing equations

Let us consider the incompressible flow of a newtonian viscous fluid with kinematic viscosity ν in an annular cavity defined by the axial gap e and by the inner radius R_1 and the outer radius R_2 (see figure 1). The motion is induced by the rotation at constant angular velocity Ω of one of the two disks, the other being kept fixed. Under the assumption of axisymmetry, the governing equations in cylindrical coordinates (r, θ, z) read:

$$\frac{1}{r} \frac{\partial r u}{\partial r} + \frac{\partial w}{\partial z} = 0 \quad (1)$$

$$\frac{\partial u}{\partial t} + \frac{1}{r} \frac{\partial r u u}{\partial r} + \frac{\partial u w}{\partial z} - \frac{v^2}{r} = -\frac{\partial P}{\partial r} + \frac{1}{Re} \left(\frac{1}{r} \frac{\partial}{\partial r} \left(r \frac{\partial u}{\partial r} \right) - \frac{u}{r^2} + \frac{\partial^2 u}{\partial z^2} \right) \quad (2)$$

$$\frac{\partial v}{\partial t} + \frac{1}{r} \frac{\partial r u v}{\partial r} + \frac{\partial v w}{\partial z} + \frac{u v}{r} = \frac{1}{Re} \left(\frac{1}{r} \frac{\partial}{\partial r} \left(r \frac{\partial v}{\partial r} \right) - \frac{v}{r^2} + \frac{\partial^2 v}{\partial z^2} \right) \quad (3)$$

$$\frac{\partial w}{\partial t} + \frac{1}{r} \frac{\partial r u w}{\partial r} + \frac{\partial w w}{\partial z} = -\frac{\partial P}{\partial z} + \frac{1}{Re} \left(\frac{1}{r} \frac{\partial}{\partial r} \left(r \frac{\partial w}{\partial r} \right) + \frac{\partial^2 w}{\partial z^2} \right) \quad (4)$$

where u, v, w are the radial, azimuthal and axial components of the velocity and P is the pressure. Note that the equations have been cast in conservative form which allows to take advantage of the finite volume formulation on a staggered mesh. These nondimensional equations were obtained by using e as reference length, ΩR_2 as reference velocity and $1/(\Omega R_2)$ as time reference. The problem thus depends on 3 non dimensional parameters, namely the Reynolds number Re defined by $Re = \frac{\Omega e R_2}{\nu}$ and two geometrical parameters, the cavity radial aspect ratio $A = (R_2 - R_1)/e$ and the radius ratio $\delta = R_1/R_2$. The computational domain thus extends from 0 to 1 in the axial direction, and from $r_1 = \frac{A\delta}{(1-\delta)}$ to $r_2 = \frac{A}{(1-\delta)}$ in the radial direction. Throughout this work, the cavity aspect ratio A is kept equal to 5.

In order to avoid singularities in the boundary conditions, the azimuthal velocity on the inner and outer shrouds was imposed to vary linearly with respect to the axial coordinate. Placing the rotating disk at $z = 0$, the boundary conditions for the azimuthal velocity v therefore read:

$$\begin{aligned} v &= 0 \text{ on } z = 1 \\ &= r \text{ on } z = 0, \delta \leq r \leq 1 \end{aligned} \quad (5)$$

Table 1 summarizes the boundary conditions for v and w for the 4 types of conditions on

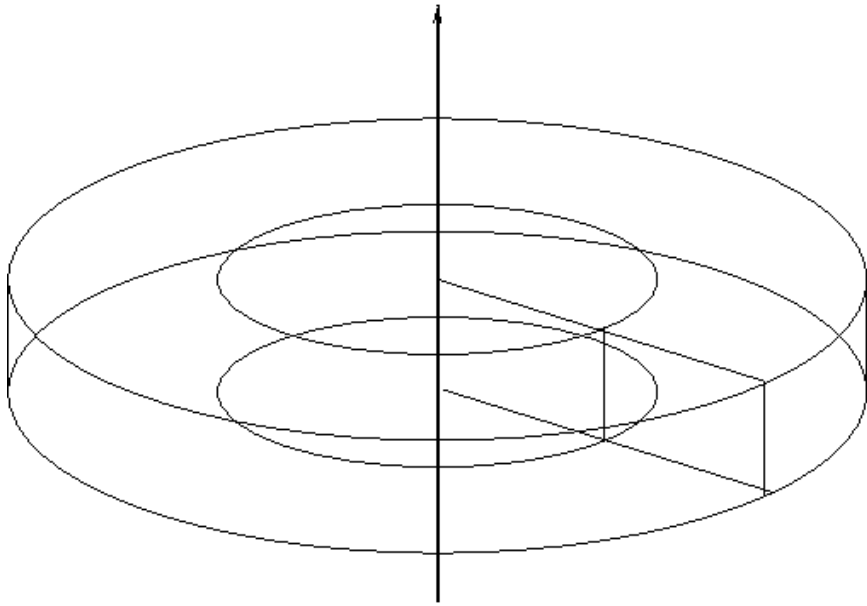


Figure 1: Schematic of the toroidal cavity

the inner hub and outer shroud. Unspecified velocity components vanish identically on the boundaries.

	ROT	FIX	LIN	STF
$R1$	$v = \delta$	$v = 0$	$v = \delta \times (1 - z)$	$\frac{\partial v}{\partial r} - \frac{v}{r} = 0 ; \frac{\partial w}{\partial r} = 0$
$R2$	$v = 1$	$v = 0$	$v = (1 - z)$	$\frac{\partial v}{\partial r} - \frac{v}{r} = 0 ; \frac{\partial w}{\partial r} = 0$

Table 1: Types of boundary condition on the inner hub BC_{R1} and outer shroud BC_{R2}

3 Numerical methods

The following results were obtained through the use of different algorithms, either time integration of the unsteady equations, linearized or fully nonlinear, direct computation of the steady equations through Newton's iterations, and computation of the leading eigenvalues of the steady solutions. All these algorithms are based on discretized equations and rely on a staggered grid arrangement of the various variables. Most computations were done with a uniform grid distribution in r and a cosine distribution in z .

3.1 Time integration of unsteady equations

The unsteady equations were integrated in time using the classical prediction-projection fractional step algorithm. The prediction step computes a provisional velocity field using

the BDF2 scheme. This velocity field is then projected onto the space of divergence free vector fields to yield the final velocity field. The projection step relies on solving an elliptic equation for the correction pressure. As always solving this equation with iterative algorithms can be time consuming, and one cannot afford to bring the residual down at machine accuracy at each time step, thereby introducing some noise in the time advancement procedure. To avoid this noise, or at least to control it, we have used different direct techniques, either LU factorization of the operator or a partial diagonalisation algorithm relying based on diagonalisation in z followed by a resolution of the tridiagonal systems in r . In both gases, the resulting divergence at the end of the each time step is at machine accuracy.

3.2 Steady state solving

Steady solutions were computed using Newton iterations with the Jacobian explicitly built in compressed COO or CSR formats. In most cases the resulting linear system was solved using the MUMPS library.

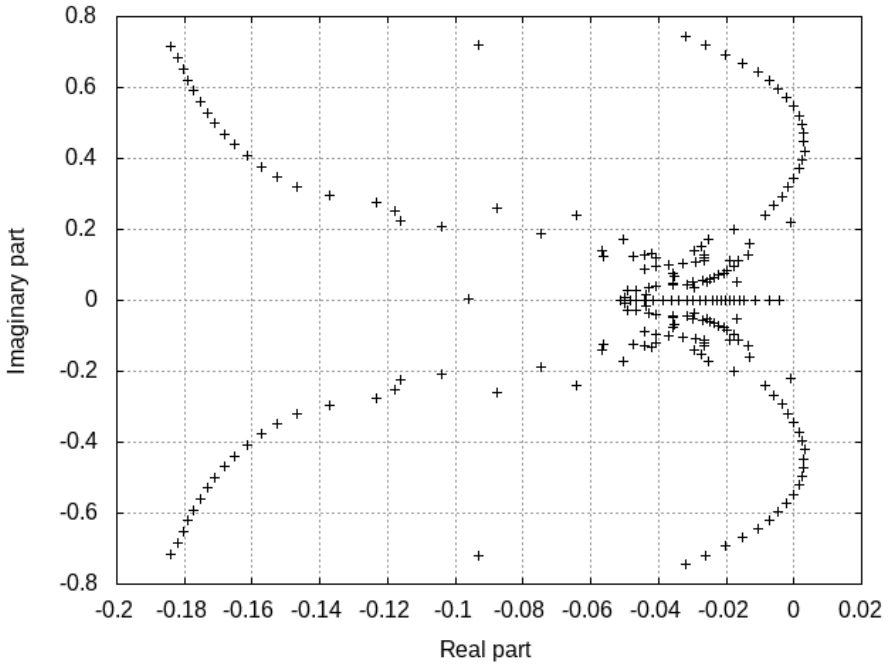
3.3 Spectrum computation

The stability of the steady solutions was determined by computing their spectrum with the help of Arpack in shift and invert mode, requiring a few tens of eigenmodes for each value of the shift. The shift and invert mode requires solving a linear system $DNL(U) - \sigma I$, where σ may be a complex shift. These were solved using the ZMUMPS routine. The numerical approximation is of finite volume on staggered grids. The results below were obtained with a grid of 256×128 with an equidistant mesh in r and a cosine distribution in z .

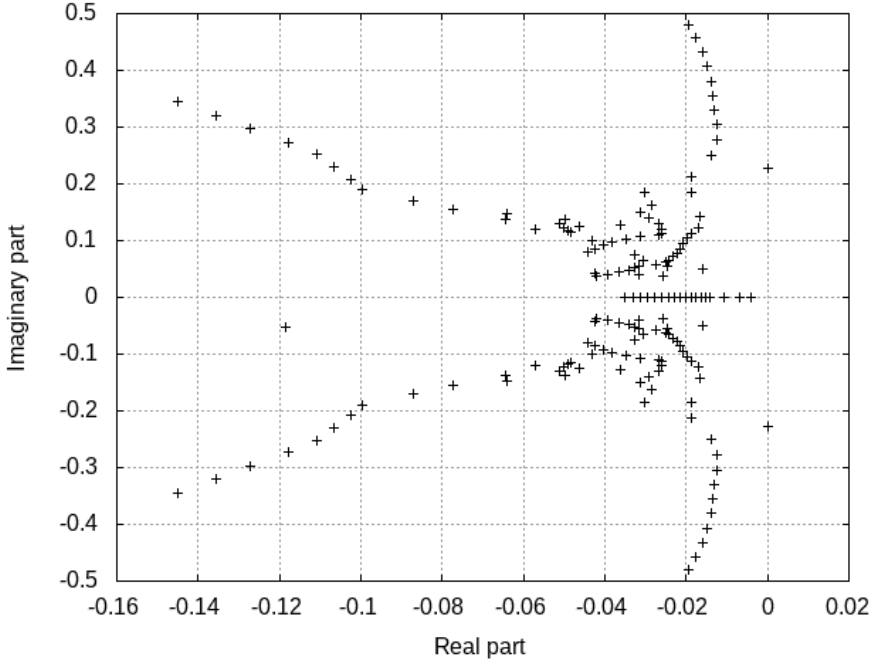
Figure 2a presents a global spectrum obtained for the following conditions : $Rf = 5$; $\delta = 0.5$, spatial resolution 256×128 , and conditions STF and LIN on the hub and shroud, respectively.

The spectrum shows that for the corresponding value of Re , the steady solution is linearly unstable several values having crossed the imaginary axis. More accurate values will be given below.

Figure 2b presents the spectrum obtained for same geometry and spatial resolution, but for conditions STF and ROT on the hub and shroud, respectively. Although quali-



(a) STF-LIN



(b) STF-ROT

Figure 2: Global spectra of steady solutions for $Rf = 5; \delta = 0.5$; 256×128 grid, equidistant in r , cosine in z . (a) Conditions STF-LIN, $Re = 7000$; (b) Conditions STF-ROT, $Re = 7800$. Spectra shown are the compound of partial spectra for different values of the shift, requiring about 50 eigenvalues each.

tatively similar, the spectra show a major distinctive feature in that while for STF-LIN, several eigenvalues cross the imaginary part almost simultaneously, for STF-ROT it is an isolated eigenvalue which is responsible for the loss of stability.

4 Numerical tests and requirements

4.1 Influence of grid resolution

It is necessary to assess the influence of grid resolution on the location of eigenvalues and hence on the value of the critical Reynolds number. These tests were performed both for STF hub and LIN shroud (figure 3), and STF-ROT (figure 4). BC conditions STF-LIN were chosen because they avoid the singularity corner and its potential influence on the grid convergence. Figure 3 first presents the evolution of the most dangerous part of the spectrum for several values of radial resolution for a fixed resolution in z equal to 128. Figure 3a shows a relative independence of the spectrum on the spatial resolution in r , increasing the resolution in r results in stabilizing the solution.

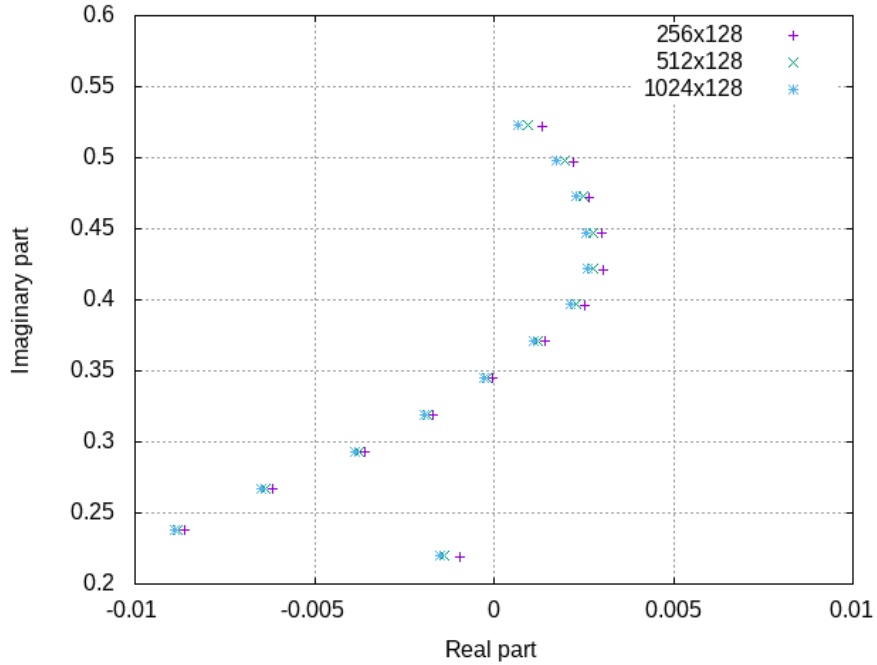
In view of the above result sensitivity of the spectrum to the resolution in z was computed for a fixed value of radial resolution of 512. On the contrary, figure 3b shows a relative large influence of the resolution in z , increasing the resolution resulting in more unstable solutions.

Similar conclusions are observed for the STF-ROT case (see figure 4), showing that the corner singularity does not have a qualitative influence on the grid sensitivity.

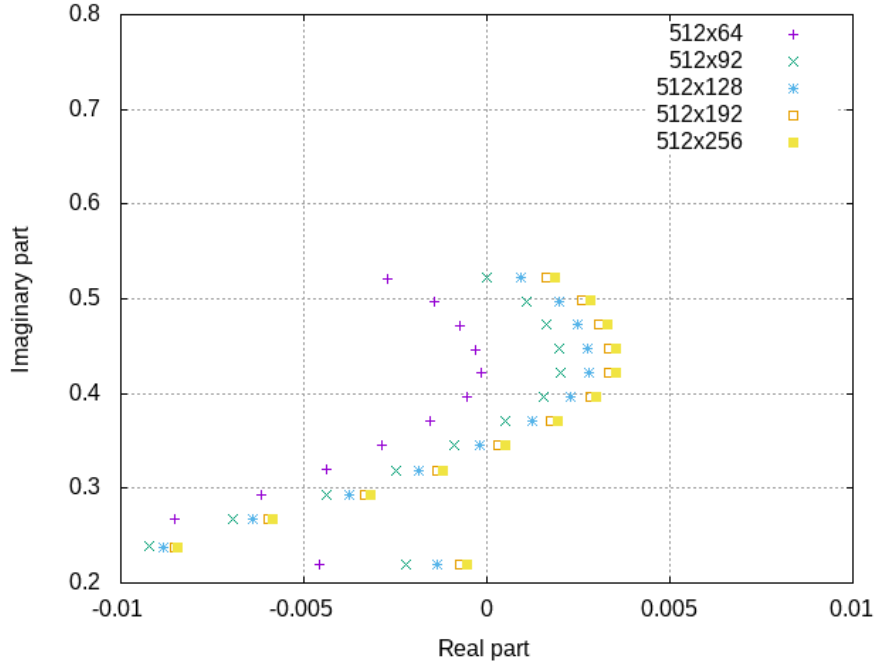
4.2 Influence of boundary conditions on hub and shroud

Table 1 shows the critical Reynolds number and corresponding angular frequency of most unstable eigenmode for the 7 types of boundary conditions investigated. These tests were performed for a grid resolution of 256×128 . They show that the most unstable configuration is a rotating hub associated to a fixed shroud, and that the most stable is the opposite, fixed hub and rotating shroud, Re_c for the latter being almost twice that of the former.

The table shows that the boundary conditions have a substantial influence, not only on the critical value, but also on the basic frequency of the unsteadiness. These values were confirmed through time integration of the linearized equations.

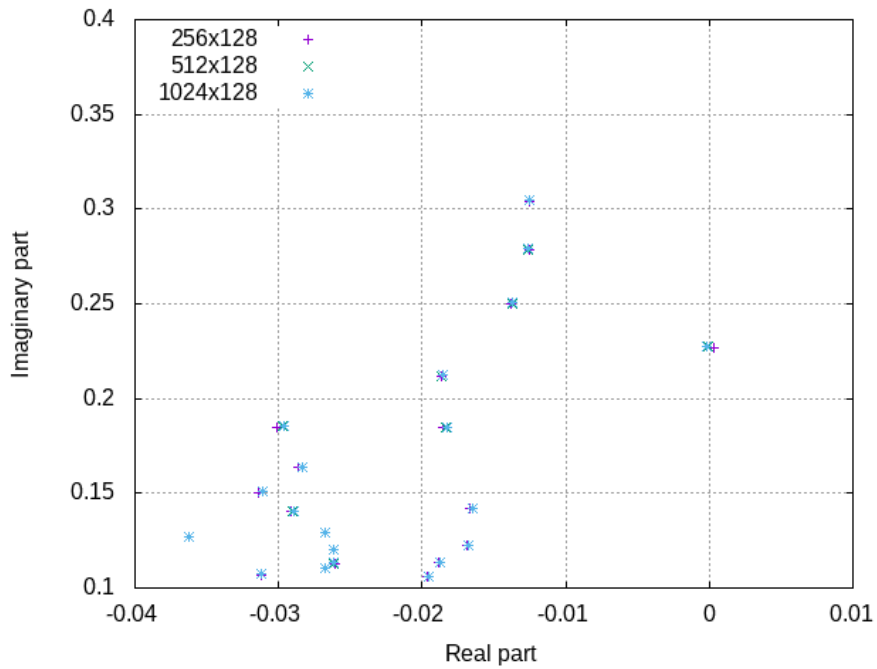


(a)

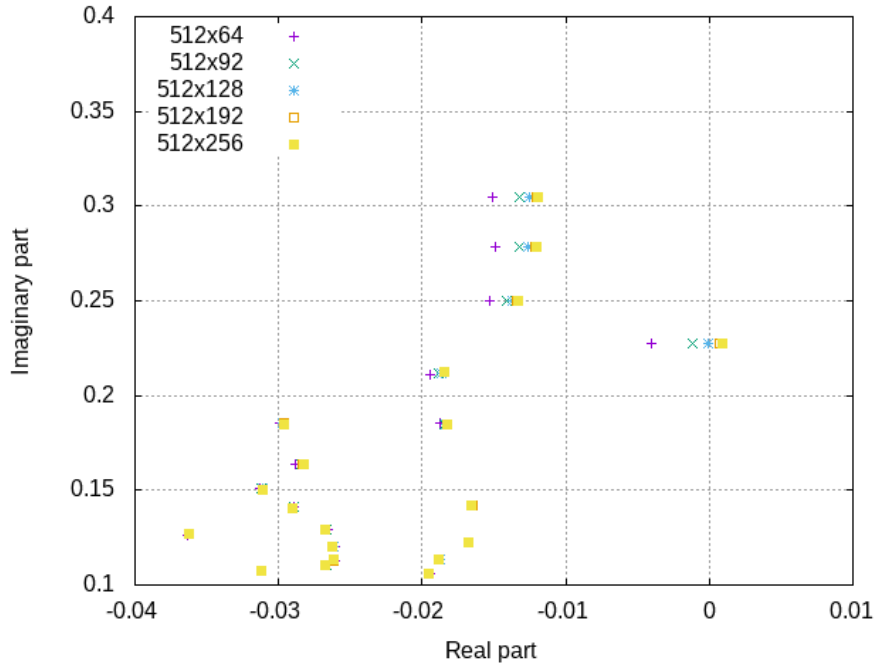


(b)

Figure 3: Evolution of part of spectrum for STF-LIN and $Re = 7000$, $Rf = 5$; $\delta = 0.5$ with spatial resolution. (a) in r for fixed value of axial resolution equal to 128. (b) in z for fixed value of radial resolution equal to 512



(a)



(b)

Figure 4: Evolution of part of spectrum for STF-ROT, for $Re = 7800$, $Rf = 5$; $\delta = 0.5$ with spatial resolution. (a) in r for fixed value of axial resolution equal to 128. (b) in z for fixed value of radial resolution equal to 512

BC_{R1}	BC_{R2}	Re_c	σ_i
ROT	FIX	4030	0.36
LIN	LIN	5315	0.3565
STF	FIX	5833	0.211
STF	LIN	6462	0.4229
STF	STF	7666	0.2255
STF	ROT	7740	0.2266
FIX	ROT	8020	0.2108

Table 2: Type of boundary condition on the inner hub BC_{R1} and outer shroud BC_{R2} ; Critical Reynolds number Re_c ; Angular frequency of most unstable eigenmode σ_i

5 Influence of curvature...

The above results have been obtained for an intermediate value of the radius ratio. It is important to understand how the situation evolves for increasing curvature effects. To this we have computed critical values and leading instability modes for decreasing values of the radius ratio δ , starting from values very close to 1, for which curvature effects can be considered as negligible. These computations were carried out for the pair of boundary conditions STF-ROT, as these are the ones that tend continuously to the case $\delta = 0$, for rotor-stator cavities with a rotating shroud. We will first show the effect on the critical value and associated eigenmode and then on the nature of the bifurcation

5.1 ...on the critical Reynolds number

5.1.1 $\delta = 0.99$

This value of δ corresponds to a cavity extending from 495 to 500 with therefore negligible curvature effects. Figure 12 displays the steady solution for $Re = 22000$, its corresponding spectrum and two selected eigenmodes. Surprisingly, the most unstable eigenmode (fig. 12c) is not a boundary layer mode, but a mode that has its maximum amplitude along the shroud. In fact this mode is reminiscent of the first instability mode that takes place in a differentially heated cavity (see [24], [25]) and is related to the corner structure that develops at the angle between the rotor and the shroud. Figure 12d shown the most unstable eigenmode boundary layer mode.

5.1.2 $\delta = 0.9$

This value of δ corresponds to a cavity extending from 45 to 50. Figure 13 displays the corresponding stability characteristics which again show that it is the corner instability

which is first responsible for the transition to unsteadiness.

5.1.3 $\delta = 0.8$

This value of δ corresponds to a cavity extending from 45 to 50. Figure 14b shows that there are two unstable eigenmodes. The high frequency mode (fig. 14c) is a boundary layer mode whereas the low frequency one (fig. 14d) corresponds to the corner instability. This value of the radius ratio thus corresponds to the critical value for which boundary layers modes take over the corner instability.

5.1.4 $\delta = 0.7$

This value of δ corresponds to a cavity extending from 11.67 to 16.67. Figure 15

5.1.5 $\delta = 0.6$

This value of δ corresponds to a cavity extending from 7.5 to 12.5. Figure 16

5.1.6 $\delta = 0.4$

This value of δ corresponds to a cavity extending from 3.33 to 8.33. Figure 17

5.1.7 $\delta = 0.3$

This value of δ corresponds to a cavity extending from 2.14 to 7.14. Figure 18

5.1.8 $\delta = 0.2$

This value of δ corresponds to a cavity extending from 1.25 to 6.25. Figure 19

5.1.9 $\delta = 0.1$

This value of δ corresponds to a cavity extending from 0.56 to 5.56. Figure 20

5.1.10 $\delta = 0.0$

This value of δ corresponds to a cavity extending from 0 to 5, a configuration that was investigated earlier. Figure 21

5.2 Numerical requirements

We have already reported in section 4.1 the great sensitivity of the spectrum to the number of grid points in the axial direction. This sensitivity even reaches the point that a too coarse resolution in z results in almost unconditionally stable solutions.

Table 3 summarizes the evolution of the critical Reynolds number and angular frequency as function of radius ratio.

$\frac{R1}{R2}$	0.99	0.9	0.8	0.7	0.6	0.5	0.4	0.3	0.2	0.1	0.
Re_c	$2.2 \cdot 10^4$	10^4	$1.2 \cdot 10^4$	9000	8700	7740	8500	10500	$1.7 \cdot 10^4$	$5.9 \cdot 10^4$	$6 \cdot 10^4$
σ_i	0.0108	0.0422	0.216	0.227	0.239	0.227	0.220	0.218	0.218	0.219	0.392

Table 3: Evolution of Critical Reynolds number Re_c and angular frequency of most unstable eigenmode σ_i with radius ratio

5.3 ...on the nature of bifurcation

In this section, we investigate the influence of the radius ratio on the nature of the bifurcation, either supercritical or subcritical. It was shown in [17] that in a cavity of radial aspect ratio 10 extending to the axis of rotation (*ie* $R1 = 0$) the Hopf bifurcation corresponding to the critical Reynolds number of 2900 is subcritical. This was done through integration of the time-dependent equations, either linearized in order to confirm the value of the critical number and to make sure that choices of the shifts in the search of eigenvalues in the shift and invert mode had not missed determinant eigenvalues, and nonlinear integration starting from linearly stable solutions as initial guess.

6 Determination of the size of the attraction basin of steady state

It is of importance to quantify the size of the attraction basin of the steady solutions. To this aim, the unsteady equations were integrated in time starting from an initial condition consisting of the steady state solution to which a centered white noise of amplitude α was added to the azimuthal velocity component. This was done for two values of Re , $4 \cdot 10^4$ and $5 \cdot 10^4$. Remember that the critical Re is close to $6 \cdot 10^4$ and that the large amplitude branch seems to fold around for $3.1 \cdot 10^4$. It was found that for $Re = 4 \cdot 10^4$, an amplitude α of $2 \cdot 10^{-7}$ was sufficient to escape the attraction basin of the steady solution, and that the amplitude decreased to $6 \cdot 10^{-9}$ for $Re = 5 \cdot 10^4$. This explains why it is almost impossible

to compute steady state solutions through time integration of the unsteady equations and increasing progressively the Reynolds number taking as initial condition a solution obtained for a smaller Re value. This is again due to the strong non-normality of the time evolution operator.

Refining α progressively lead to the identification of two edge states which display different qualitative dynamics. That for $Re = 4 \cdot 10^4$ is mono-periodic as seen from figure 22a while that for $Re = 5 \cdot 10^4$ displays a bi-periodic time evolution (figure 22b).

References

- [1] H. P. Greenspan. *The theory of rotating fluids*. Cambridge University Press, 1969.
- [2] J. Pedlovski. *Geophysical fluid dynamics*. Springer New York, NY, second edition, 1987.
- [3] J.M. Owen and R.H. Rogers. *Flow and Heat Transfer in Rotating-Disc Systems : Rotor-stator systems, volume 1*. Springer-Verlag, Berlin, 1 edition, 1989.
- [4] P. J. Zandbergen and D. Dijkstra. von Kármán swirling flows. *Ann. Rev. Fluid Mech.*, 19:465–491, 1987.
- [5] J. M. Lopez. Flow between a stationary and rotating disk shrouded by a co-rotating cylinder. *Phys. Fluids*, 8:2605–2613, 1996.
- [6] S.C. Cheah, H. Iacovides, D.C. Jackson, H. Ji, and B.E. Launder. Experimental investigation of enclosed rotor-stator disc flows. *Exp. Therm. Fluid Sci.*, 9:445–455, 1994.
- [7] G. Gauthier, P. Gondret, and M. Rabaud. Axisymmetric propagating vortices in the flow between a stationary and a rotating disk enclosed by a cylinder. *J. Fluid Mech.*, 386:105–126, 1999.
- [8] L. Schouveiler, P. Le Gal, and M. P. Chauve. Stability of a traveling roll system in a rotating disk flow. *Phys. Fluids*, 10:2695–2697, 1998.
- [9] L. Schouveiler, P. Le Gal, and M. P. Chauve. Instabilities of the flow between a rotating and a stationary disk. *J. Fluid Mech.*, 443:329–350, 2001.

- [10] J. W. Daily and R. E. Nece. Chamber dimension effects on induced flow and frictional resistance of enclosed rotating disks. *J. Basic Eng.*, 82(1):217–230, 1960.
- [11] S. Poncet, E. Serre, and P. Le Gal. Revisiting the two first instabilities of the flow in an annular rotor-stator cavity. *Phys. Fluids*, 21:064106(8), 2009.
- [12] E. Severac, S. Poncet, E. Serre, and M.-P. Chauve. Large eddy simulation and measurements of turbulent enclosed rotor-stator flows. *Phys. Fluids*, 19(085113):1–16, 2007.
- [13] J. M. Lopez and J. Shen. An efficient spectral-projection method for the Navier-Stokes equations in cylindrical geometries: I. Axisymmetric cases. *J. Comput. Phys.*, 139:308–326, 1998.
- [14] E. Serre and J.-P. Pujicani. A three-dimensional pseudospectral method for rotating flows in a cylinder. *Computers & Fluids*, 30:491–519, 2001.
- [15] A. Y. Gelfgat. Primary oscillatory instability in a rotating disk-cylinder system with aspect (height/radius) ratio varying from 0.1 to 1. *Fluid Dyn. Res.*, 47:035502(14), 2015.
- [16] A. Cros, E. Floriani, P. Le Gal, and R. Lima. Transition to turbulence of the Batchelor flow in a rotor/stator device. *Eur. J. Mech. B/Fluids*, 24:409–424, 2005.
- [17] O. Daube and P. Le Quéré. Numerical investigation of the first bifurcation for the flow in a rotor-stator cavity of radial aspect ratio 10. *Computers & Fluids*, 31:481–494, 2002.
- [18] L.S. Tuckerman and D. Barkley. Bifurcation analysis for timesteppers. In E. Doedel and L.S. Tuckerman, editors, *Numerical Methods for Bifurcation Problems and Large-Scale Dynamical Systems*, pages 453–466. Springer, New York, 2000.
- [19] E. Serre, E. Tuliszka-Sznitko, and P. Bontoux. Coupled numerical and theoretical study of the flow transition between a rotating and a stationary disk. *Phys. Fluids*, 16:688–706, 2004.
- [20] J. M. Lopez, F. Marques, A. M. Rubio, and M. Avila. Crossflow instability of finite Bödewadt flows : Transients and spiral waves. *Phys. Fluids*, 21:114107, 2009.

- [21] M. Queguineur, T. Bridel-Bertomeu, L. Gicquel, and G. Staffelbach. Large eddy simulations and global stability analyses of an annular and cylindrical rotor-stator cavity limit cycles. *Phys. Fluids*, 31(104109):1–18, 2019.
- [22] S. Makino, M. Iganaki, and M. Nakagawa. Laminar-turbulence transition over the rotor disk in an enclosed rotor-stator cavity. *Flow Turb. Comb.*, 95:399–413, 2015.
- [23] G. Veronis. The analogy between rotating and stratified fluids. *Ann. Rev. Fluid Mech.*, 2:37–66, 1970.
- [24] P. Le Quéré and M. Behnia. From onset of unsteadiness to chaos in a differentially heated square cavity. *J. Fluid Mech.*, 359:81–107, 1998.
- [25] S. Xin and P. Le Quéré. Natural convection flows in air-filled differentially heated cavities with adiabatic horizontal walls. *Numer. Heat Transfer A*, 50(5):437–466, 2006.

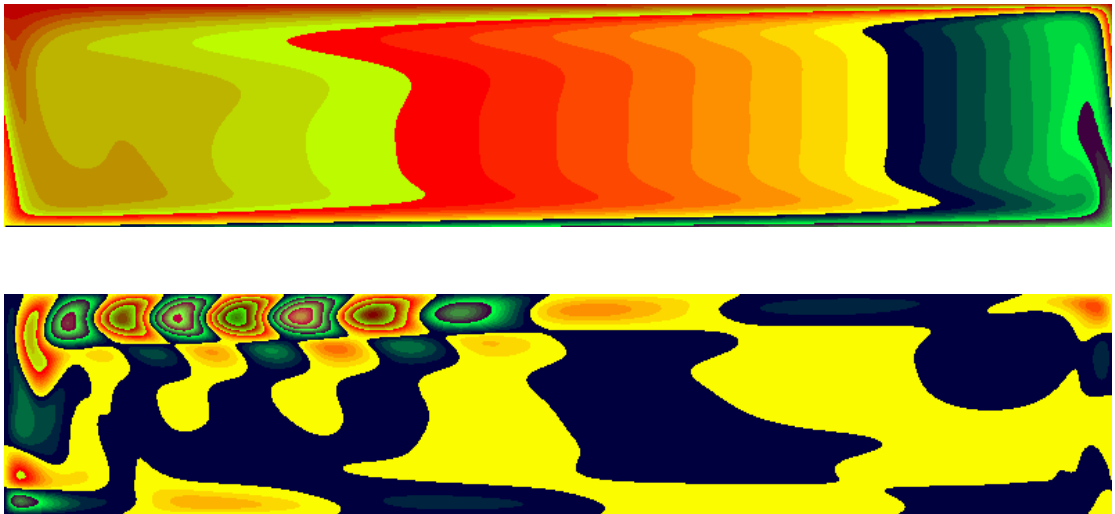


Figure 5: Boundary conditions : LIN-LIN. Steady azimuthal velocity and corresponding eigenmode (real part) corresponding to the eigenvalue $(-0.0343+i 0.0735)$ in the spectrum

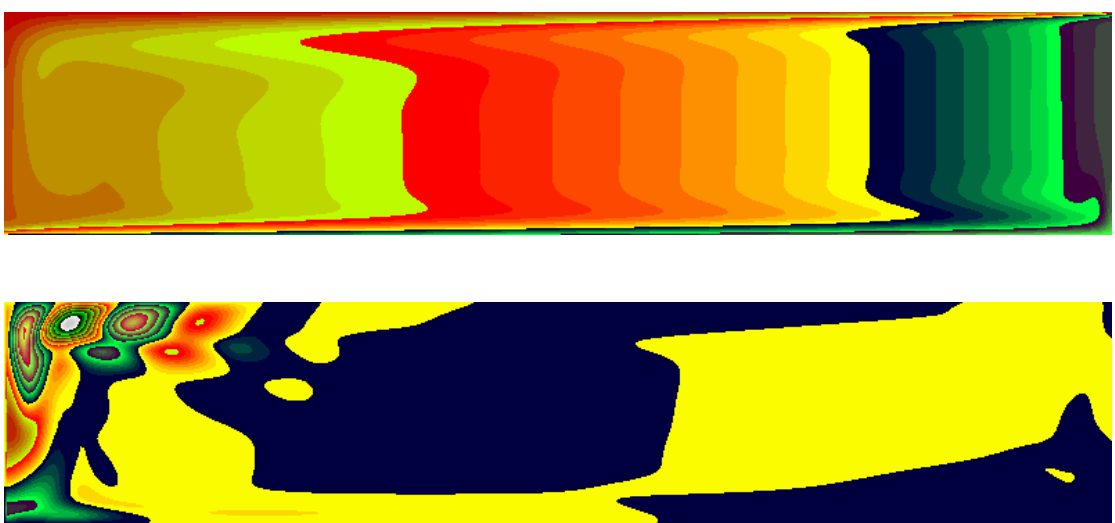


Figure 6: Boundary conditions : STF-STF. Steady azimuthal velocity and corresponding eigenmode (real part) corresponding to the eigenvalue $(-0.0343+i 0.0735)$ in the spectrum

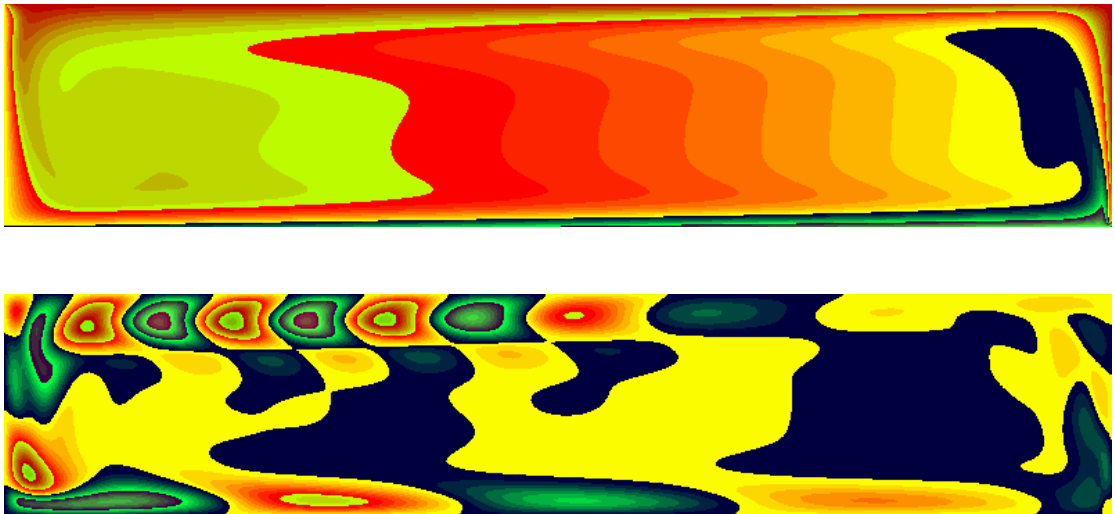


Figure 7: Boundary conditions : ROT-FIX. Steady azimuthal velocity and corresponding eigenmode (real part) corresponding to the eigenvalue $(-0.0343+i 0.0735)$ in the spectrum

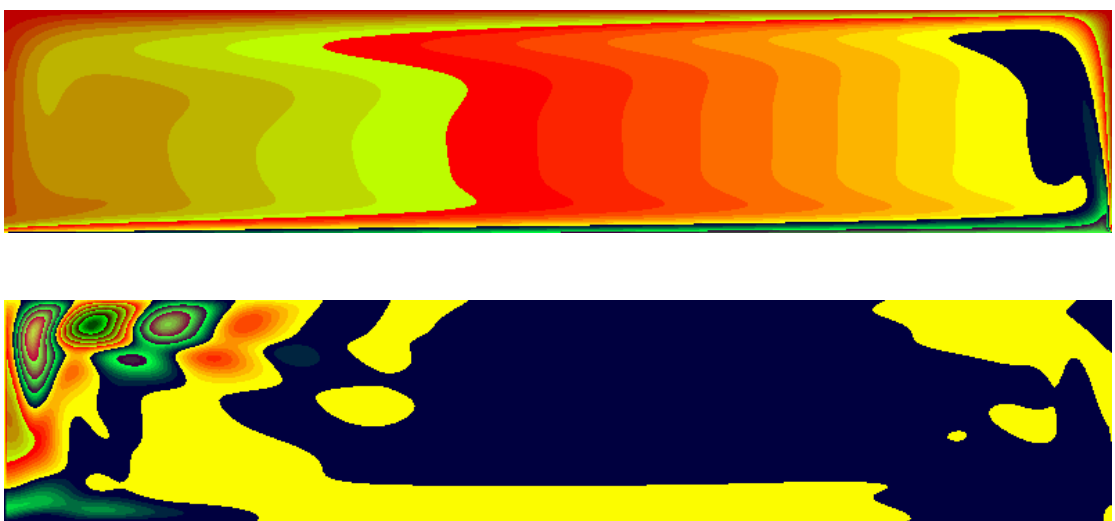


Figure 8: Boundary conditions : STF-FIX. Steady azimuthal velocity and corresponding eigenmode (real part) corresponding to the eigenvalue $(-0.0343+i 0.0735)$ in the spectrum

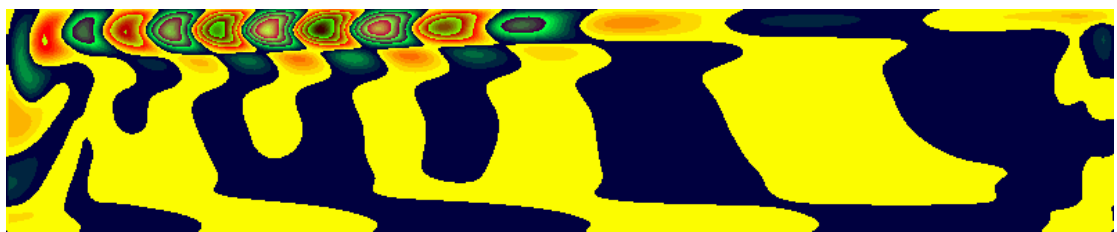
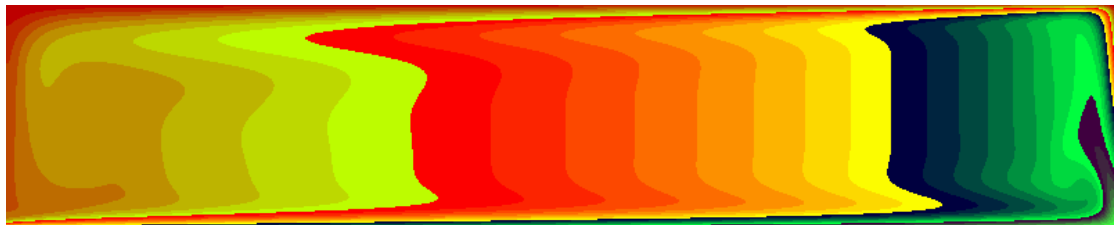


Figure 9: Boundary conditions : STF-LIN. Steady azimuthal velocity field and corresponding eigenmode (real part) corresponding to the eigenvalue $(-0.0343 + i 0.0735)$ in the spectrum

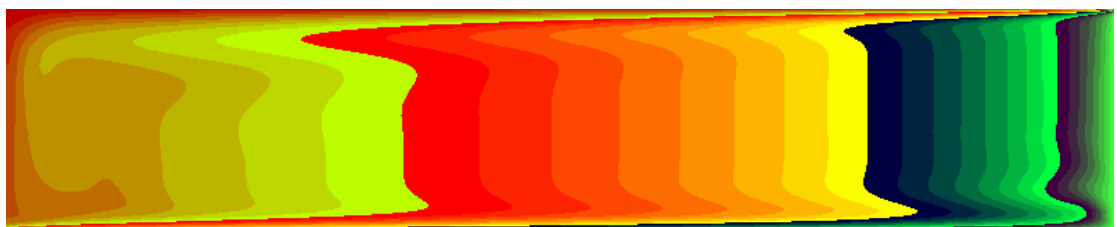


Figure 10: Boundary conditions : STF-ROT. Steady azimuthal velocity and corresponding eigenmode (real part) corresponding to the eigenvalue $(-0.0343 + i 0.0735)$ in the spectrum

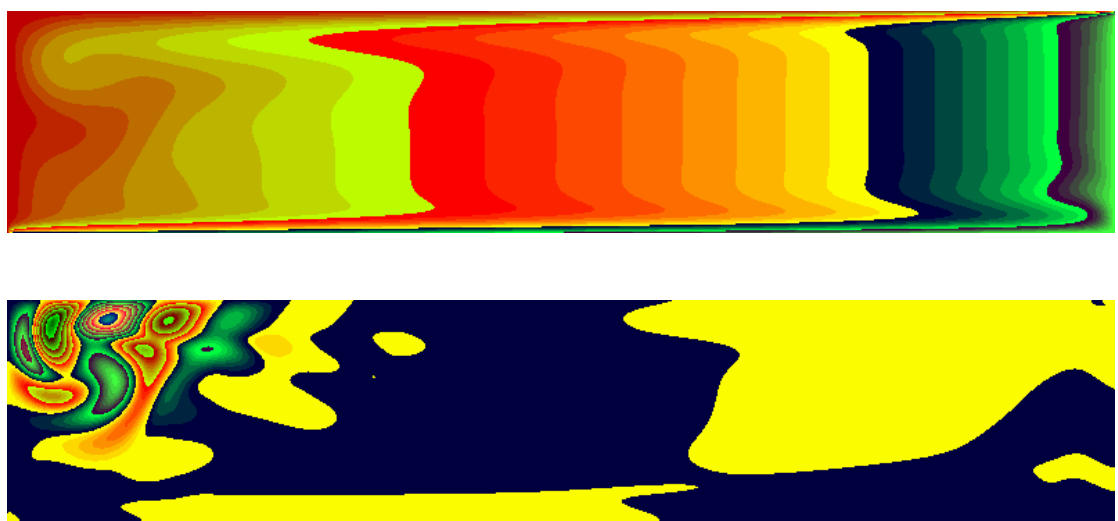
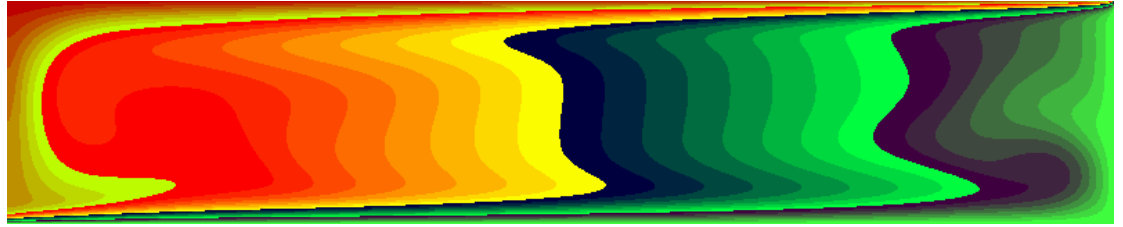
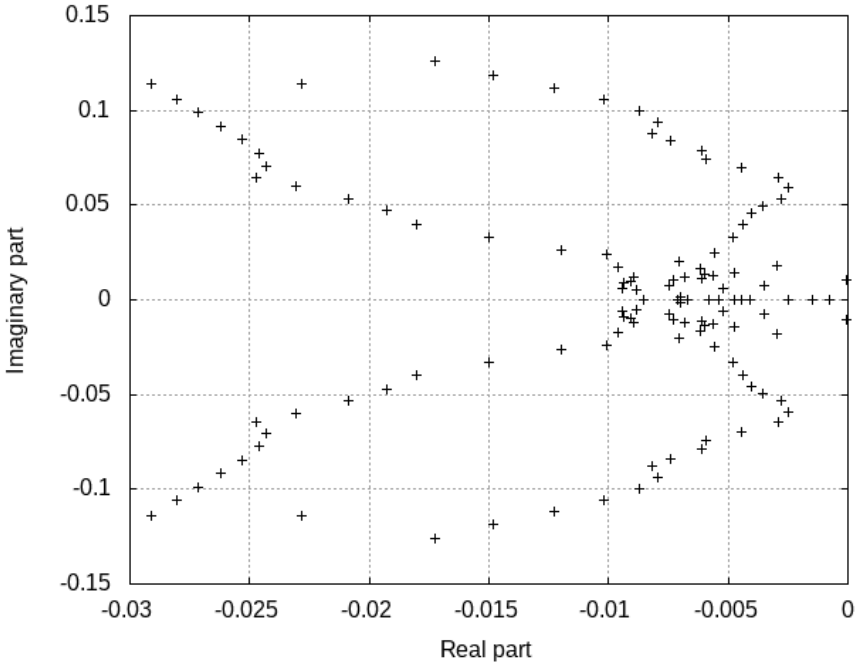


Figure 11: Boundary conditions : FIX-ROT. Steady azimuthal velocity and corresponding eigenmode (real part) corresponding to the eigenvalue $(-0.0343+i 0.0735)$ in the spectrum



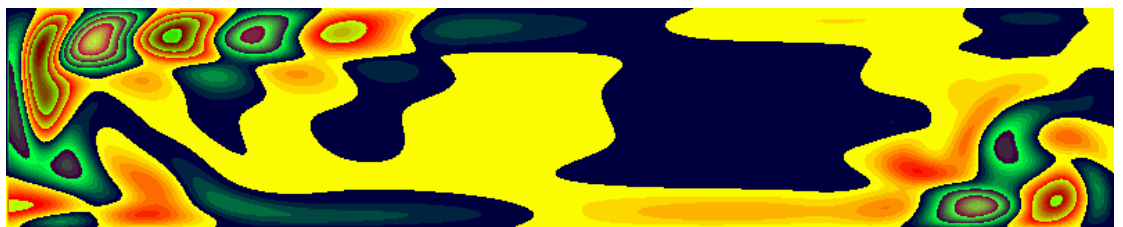
(a) Steady solution $Re = 22000$



(b) Corresponding spectrum

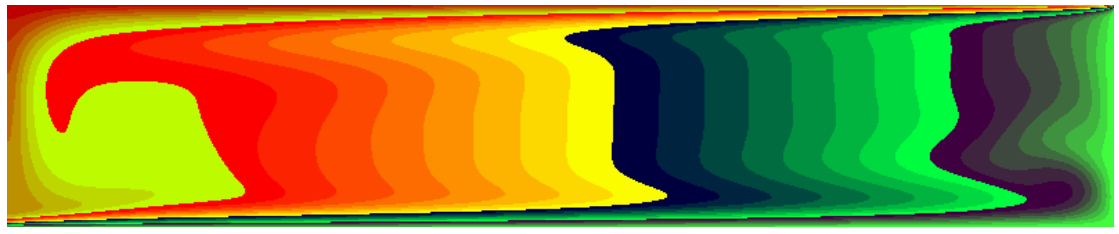


(c) Eigenmode corresponding to $(\sigma_r, \sigma_i) = (-8 \cdot 10^{-5}, 0.0108)$

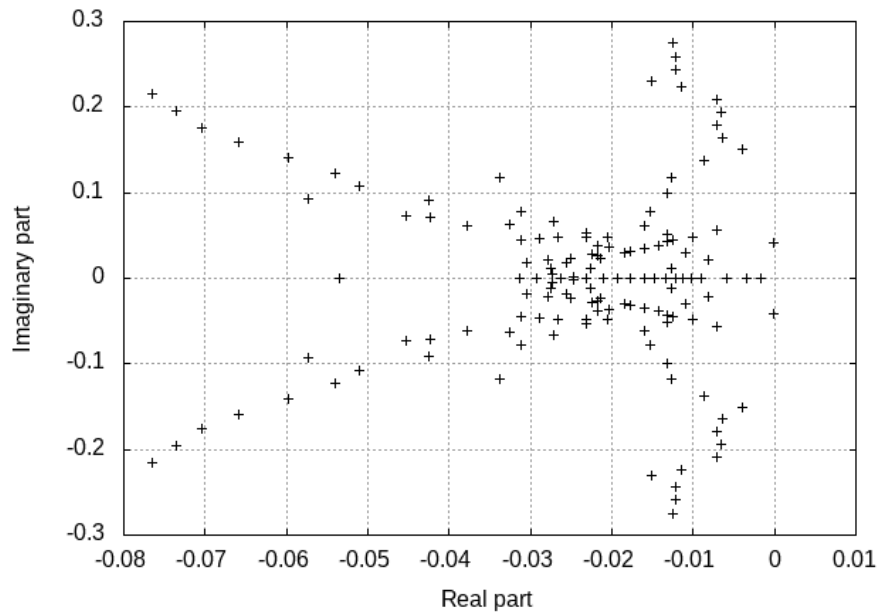


(d) Eigenmode corresponding to $(\sigma_r, \sigma_i) = (-2.9 \cdot 10^{-3}, 0.0646)$

Figure 12: Steady solution for $Rf = 5; \delta = 0.99$; $Re = 22000$; Conditions STF-ROT ; 256×128 grid, equidistant in r , cosine in z . From top to bottom : steady solution, corresponding spectrum, most unstable eigenmode, most unstable boundary layer eigenmode



(a) Steady solution $Re = 10^4$

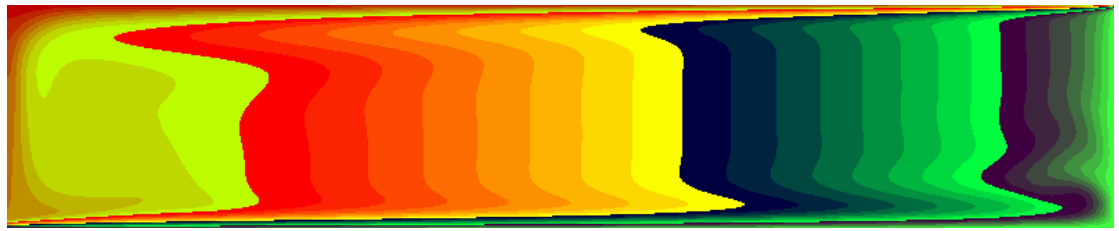


(b) Corresponding spectrum

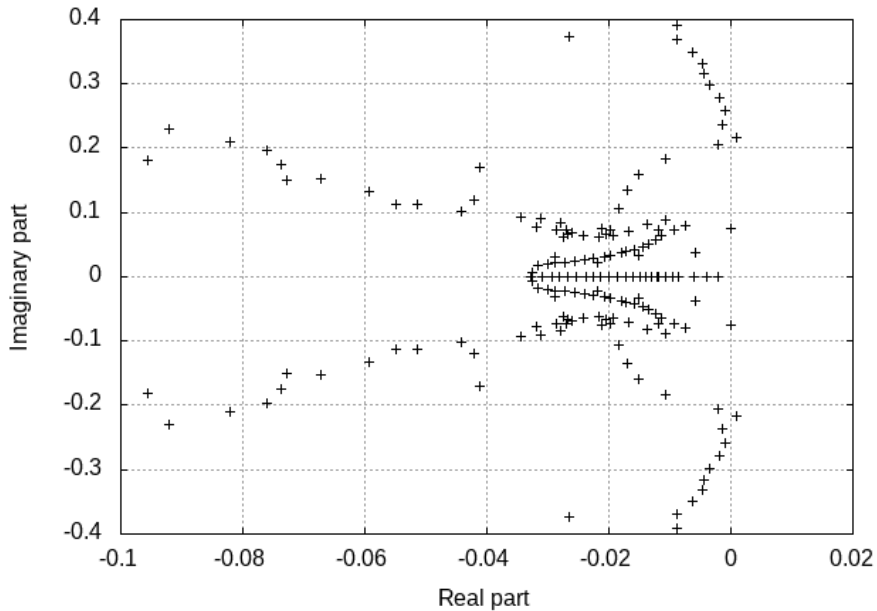


(c) Eigenmode corresponding to $(\sigma_r, \sigma_i) = (-7 \cdot 10^{-5}, 0.0422)$

Figure 13: Steady solution for $Rf = 5; \delta = 0.9$; $Re = 10^4$; Conditions STF-ROT ; 256×128 grid, equidistant in r , cosine in z . From top to bottom : steady solution, corresponding spectrum, most unstable eigenmode



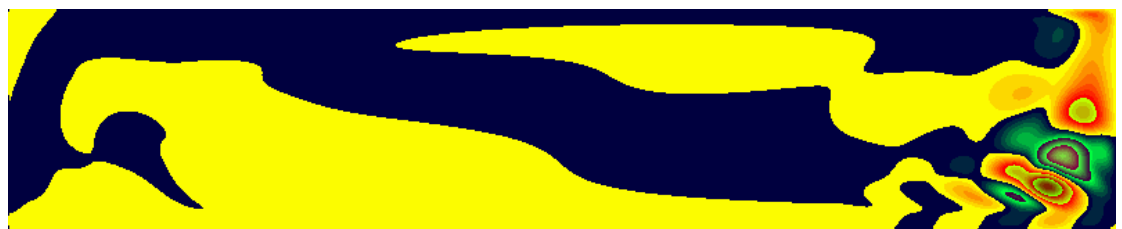
(a) Steady solution $Re = 12000$



(b) Corresponding spectrum

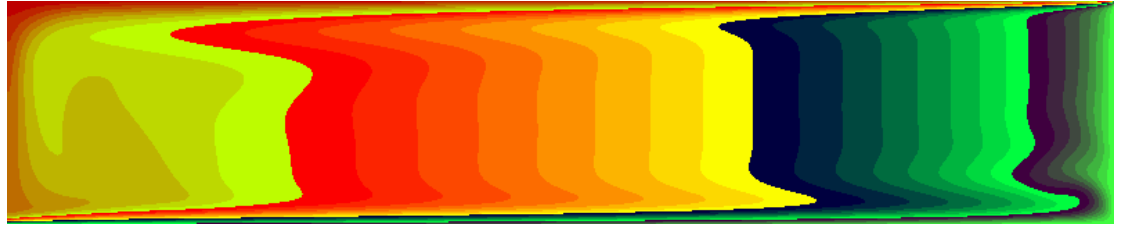


(c) Eigenmode corresponding to $(\sigma_r, \sigma_i) = (8.8 \cdot 10^{-4}, 0.216)$

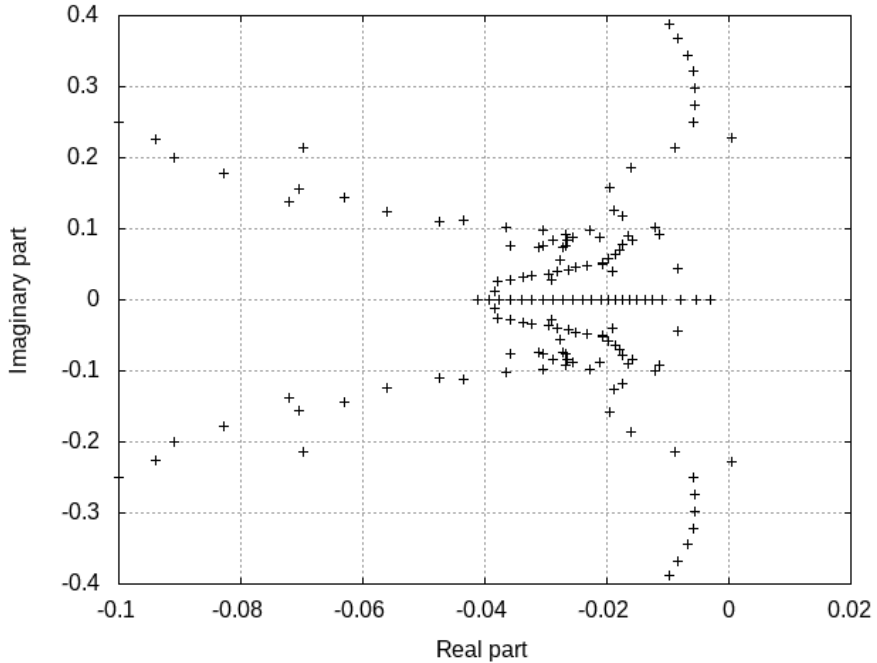


(d) Eigenmode corresponding to $(\sigma_r, \sigma_i) = (3.2 \cdot 10^{-5}, 0.0743)$

Figure 14: Steady solution for $Rf = 5; \delta = 0.8$; $Re = 12000$; Conditions STF-ROT ; 256×128 grid, equidistant in r , cosine in z . From top to bottom : steady solution, corresponding spectrum, most unstable eigenmode, low frequency eigenmode



(a) Steady solution $Re = 9000$



(b) Corresponding spectrum

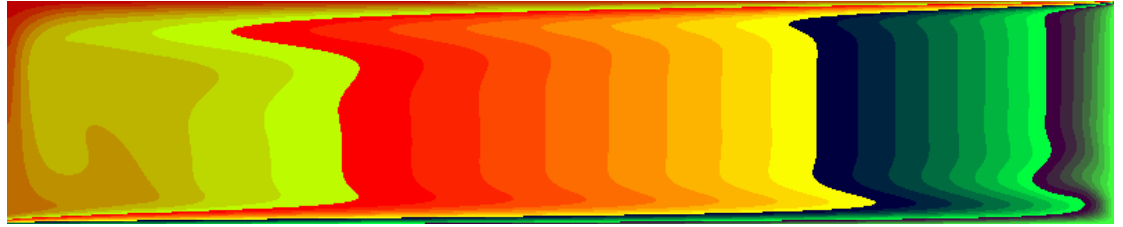


(c) eigenmode corresponding to $(\sigma_r, \sigma_i) = (5.5 \cdot 10^{-4}, 0.227)$

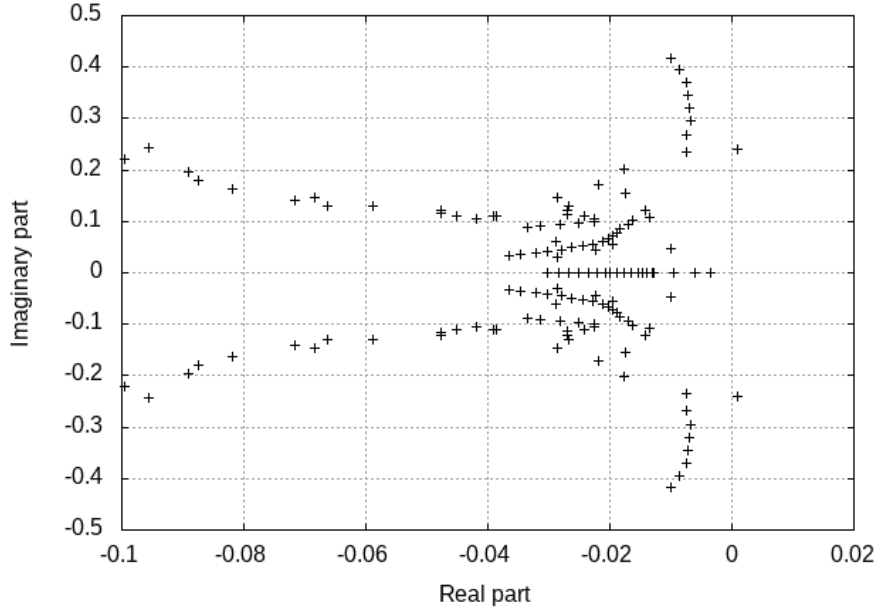


(d) Eigenmode corresponding to $(\sigma_r, \sigma_i) = (-2.9 \cdot 10^{-3}, 0.)$

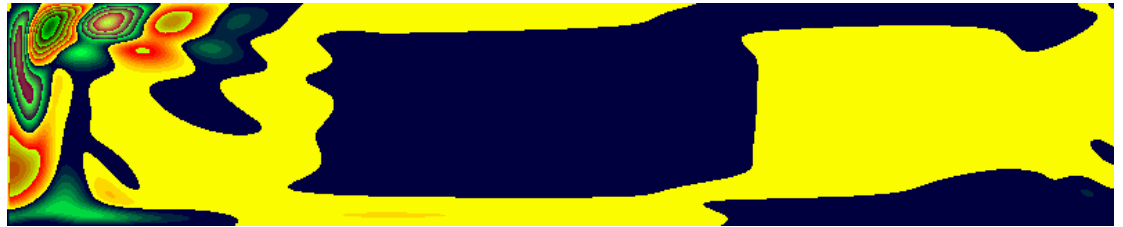
Figure 15: Steady solution for $Rf = 5; \delta = 0.7 ; Re = 9000$; Conditions STF-ROT ; 256×128 grid, equidistant in r , cosine in z . From top to bottom : steady solution, corresponding spectrum, most unstable eigenmode, least stable stationary eigenmode



(a) Steady solution $Re = 8700$



(b) Corresponding spectrum

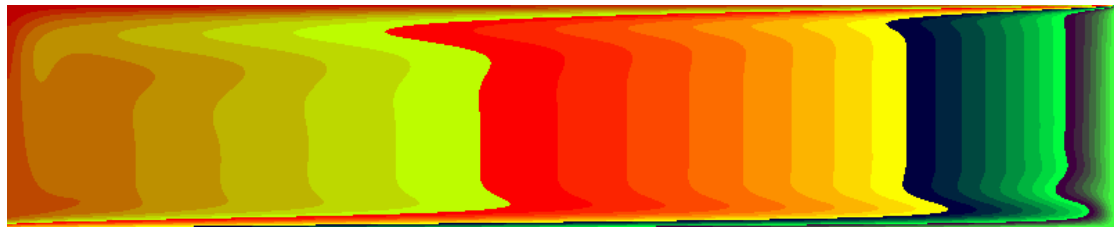


(c) eigenmode corresponding to $(\sigma_r, \sigma_i) = (1.10^{-3}, 0.239)$

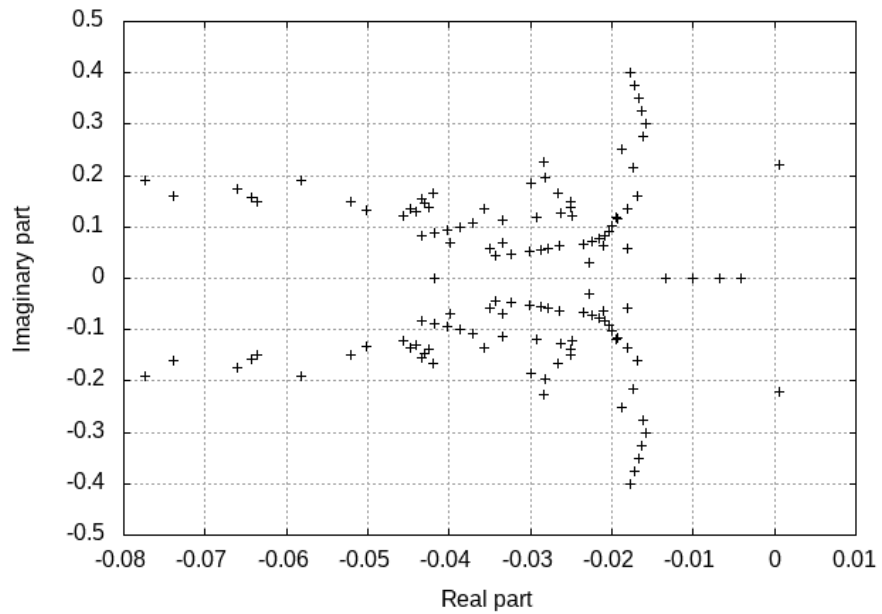


(d) Eigenmode corresponding to $(\sigma_r, \sigma_i) = (-3.4 \cdot 10^{-3}, 0.)$

Figure 16: Steady solution for $Rf = 5; \delta = 0.6 ; Re = 9000$; Conditions STF-ROT ; 256×128 grid, equidistant in r , cosine in z . From top to bottom : steady solution, corresponding spectrum, most unstable eigenmode, least stable stationary eigenmode



(a) Steady solution $Re = 8500$

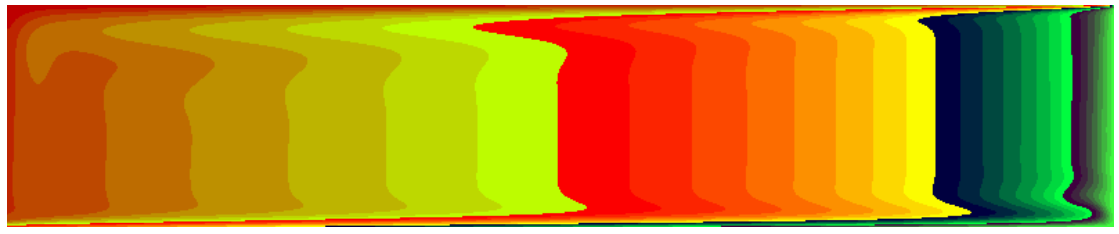


(b) Corresponding spectrum

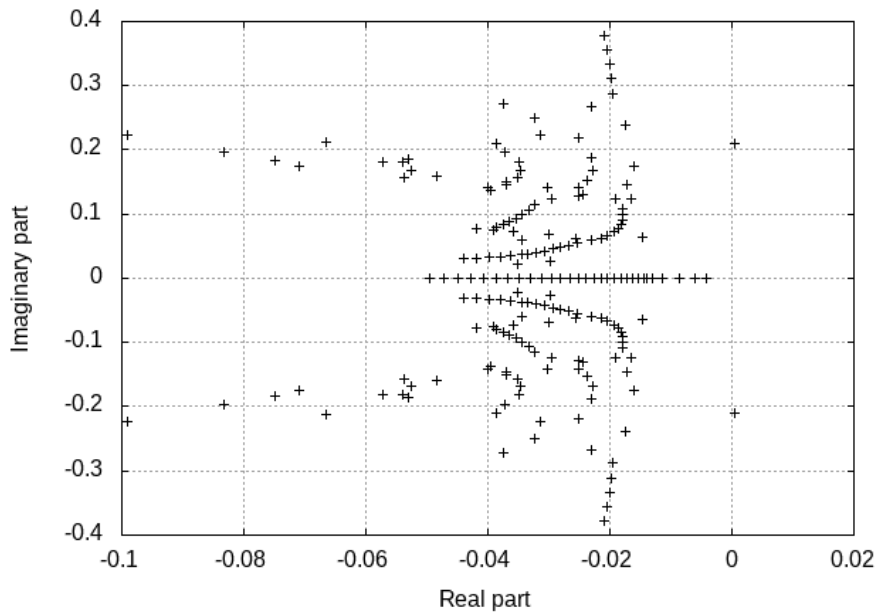


(c) Eigenmode corresponding to $(\sigma_r, \sigma_i) = (6.6 \cdot 10^{-4}, 0.220)$

Figure 17: Steady solution for $Rf = 5; \delta = 0.4$; $Re = 8500$; Conditions STF-ROT ; 256×128 grid, equidistant in r , cosine in z . From top to bottom : steady solution, corresponding spectrum, most unstable eigenmode



(a) Steady solution $Re = 10500$

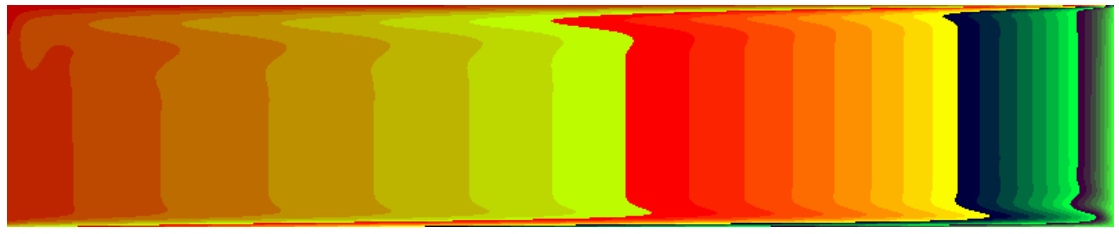


(b) Corresponding spectrum

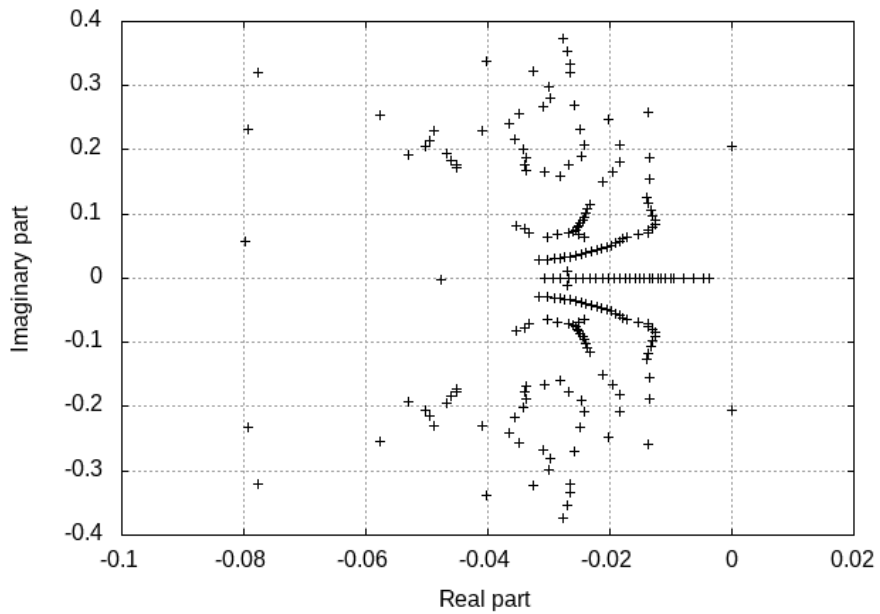


(c) Eigenmode corresponding to $(\sigma_r, \sigma_i) = (5.1 \cdot 10^{-4}, 0.218)$

Figure 18: Steady solution for $Rf = 5; \delta = 0.3$; $Re = 10500$; Conditions STF-ROT ; 256×128 grid, equidistant in r , cosine in z . From top to bottom : steady solution, corresponding spectrum, most unstable eigenmode



(a) Steady solution $Re = 17000$

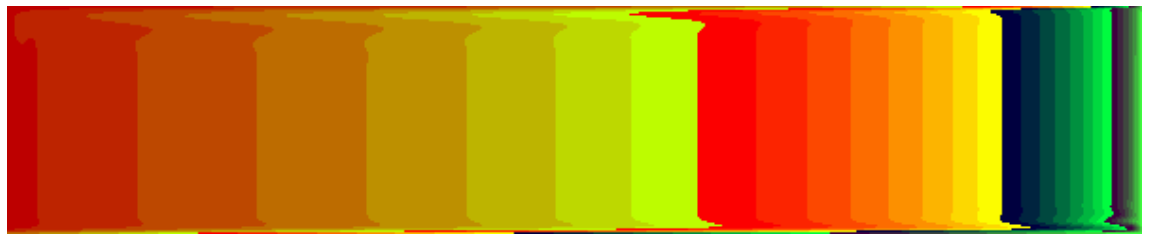


(b) Corresponding spectrum

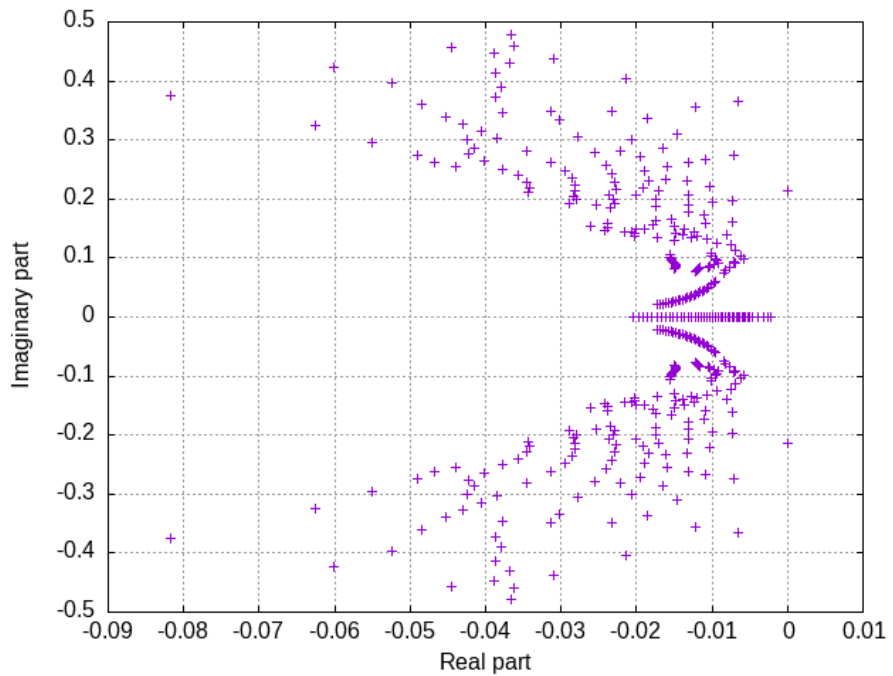


(c) Eigenmode corresponding to $(\sigma_r, \sigma_i) = (-1.1 \cdot 10^{-4}, 0.2057)$

Figure 19: Steady solution for $Rf = 5; \delta = 0.2$; $Re = 17000$; Conditions STF-ROT ; 256×128 grid, equidistant in r , cosine in z . From top to bottom : steady solution, corresponding spectrum, most unstable eigenmode



(a) Steady solution $Re = 54000$



(b) Corresponding spectrum

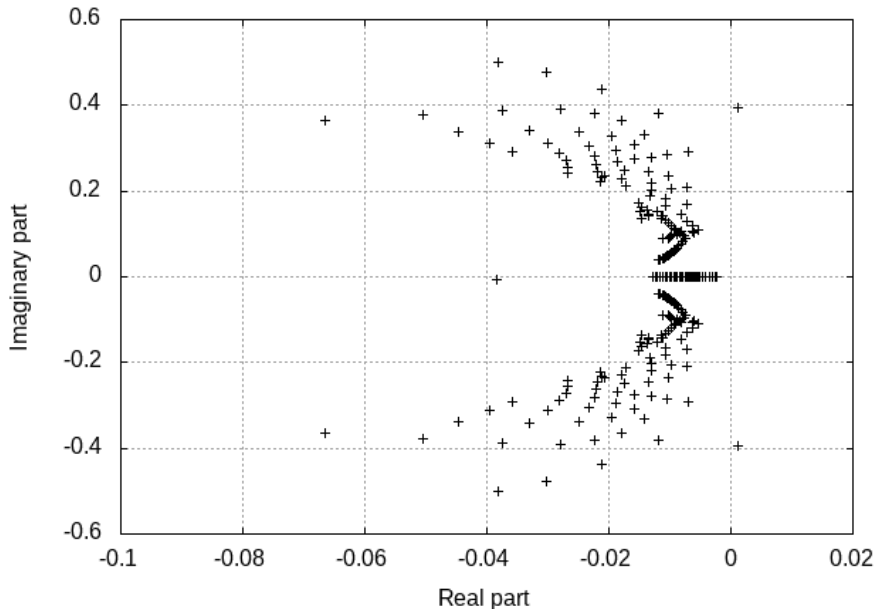


(c) Eigenmode corresponding to $(\sigma_r, \sigma_i) = (6.9 \cdot 10^{-5}, 0.213)$

Figure 20: Steady solution for $Rf = 5; \delta = 0.1$; $Re = 54000$; Conditions STF-ROT ; 512×192 grid, equidistant in r , cosine in z . From top to bottom : steady solution, corresponding spectrum, most unstable eigenmode



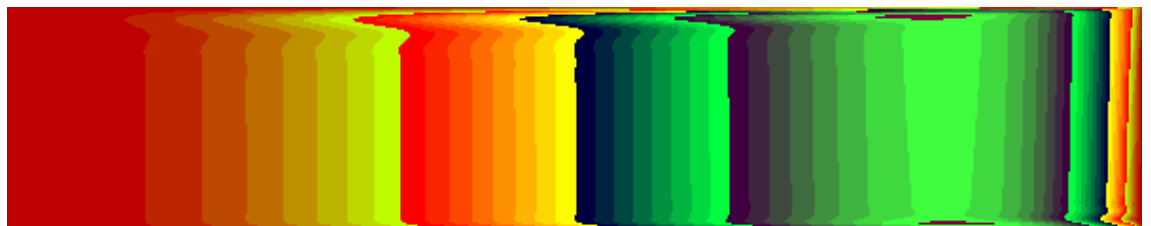
(a) Steady solution $Re = 60000$



(b) Corresponding spectrum

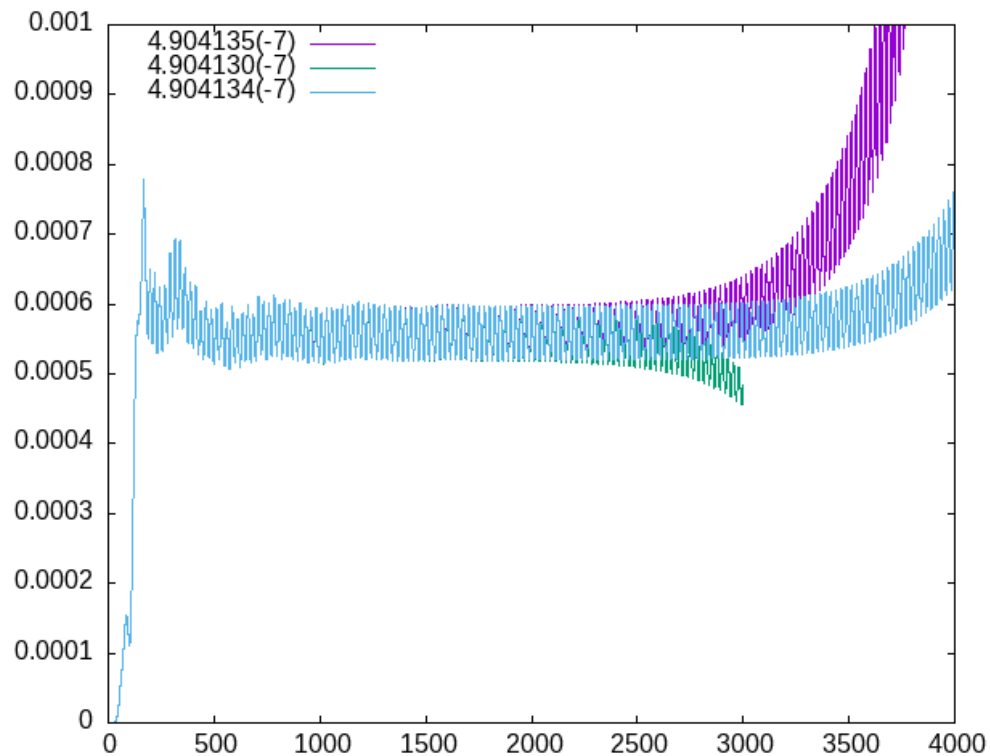


(c) Eigenmode corresponding to $(\sigma_r, \sigma_i) = (2.2 \cdot 10^{-3}, 0.392)$

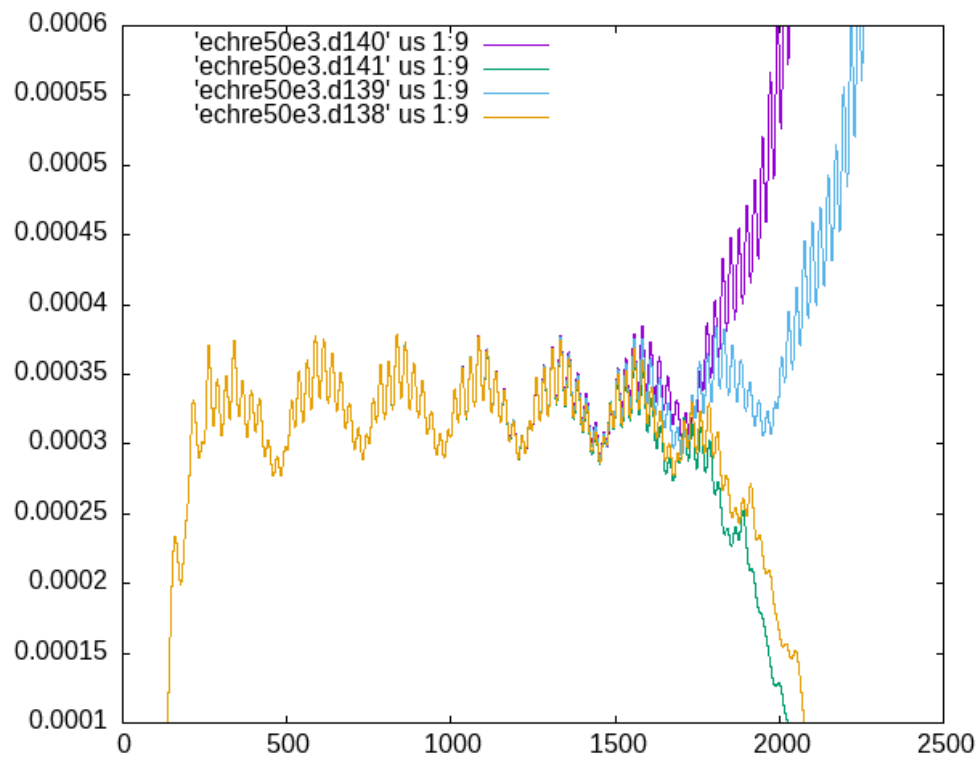


(d) Eigenmode corresponding to $(\sigma_r, \sigma_i) = (2.2 \cdot 10^{-3}, 0.392)$

Figure 21: Steady solution for $Rf = 5; \delta = 0.0$; $Re = 60000$; Conditions STF-ROT ; 512×256 grid, equidistant in r , cosine in z . From top to bottom : steady solution, corresponding spectrum, most unstable eigenmode



(a) $Re = 40000$



(b) $Re = 50000$

Figure 22: Bisection $Rf = 5; \delta = 0.0$; Conditions STF-ROT; 512×256 grid, equidistant in r , cosine in z .